HHS Public Access

Author manuscript

*J Physiol*. Author manuscript; available in PMC 2020 August 18.

Published in final edited form as:

*J Physiol*. 2020 April ; 598(7): 1327–1338. doi:10.1113/JP277083.

# Quantitative tests reveal that microtubules tune the healthy heart but underlie arrhythmias in pathology

**Humberto C. Joca**[1], **Andrew K. Coleman**[1], **Chris W. Ward**[2], **George S. B. Williams**[1]

[1]Centre for Biomedical Engineering and Technology, University of Maryland School of Medicine, Baltimore, MD, USA

[2]Department of Orthopedics, University of Maryland School of Medicine, Baltimore, MD, USA

## Abstract

Microtubule (MT) mechanotransduction links diastolic stretch to generation of NADPH oxidase 2 (NOX2)-dependent reactive oxygen species (ROS), signals we term X-ROS. While stretch-elicited X-ROS primes intracellular calcium ($Ca^{2+}$) channels for synchronized activation in the healthy heart, the dysregulated excess in this pathway underscores asynchronous $Ca^{2+}$ release and arrhythmia. Here, we expanded our existing computational models of $Ca^{2+}$ signalling in heart to include MT-dependent mechanotransduction through X-ROS. Informed by new focused experimental tests to properly constrain our model, we quantify the role of X-ROS on excitation-contraction coupling in healthy and pathological conditions. This approach allowed for a mechanistic investigation that revealed new insights into X-ROS signalling in disease including changes in MT network density and post-translational modifications (PTMs), elevated NOX2 expression, altered $Ca^{2+}$ release dynamics (i.e. $Ca^{2+}$ sparks and $Ca^{2+}$ waves), how NOX2 is activated by and responds to stretch, and finally the degree to which normalizing X-ROS can prevent $Ca^{2+}$-dependent arrhythmias.

## Introduction

Cardiac excitation-contraction coupling (ECC) is governed by voltage-dependent calcium ($Ca^{2+}$) influx that rapidly activates $Ca^{2+}$ sparks, the elementary $Ca^{2+}$ release events arising from clusters of type 2 ryanodine receptor (RyR2) $Ca^{2+}$ channels in the sarcoplasmic reticulum (SR) membrane (Cheng *et al.* 1993; Cheng & Lederer, 2008). Informed by experimental measures, computational models of $Ca^{2+}$ sparks and cardiac SR $Ca^{2+}$ release



**Corresponding authors** G. S. B. Williams: Centre for Biomedical Engineering and Technology, University of Maryland School of Medicine, Baltimore, MD, USA. gswill@umaryland.edu, C. W. Ward: Department of Orthopedics, University of Maryland School of Medicine, Baltimore, MD, USA. ward@umaryland.edu.

Author contributions

H.C.J., C.W.W. and G.S.B.W. contributed to the design of the work; acquisition, analysis, and interpretation of the data; and drafting of the manuscript. A.K.C. contributed to acquisition and analysis of data. All authors have read and approved the final version of this manuscript and agree to be accountable for all aspects of the work in ensuring that questions related to the accuracy or integrity of any part of the work are appropriately investigated and resolved. All persons designated as authors qualify for authorship, and all those who qualify for authorship are listed. C.W.W. and G.S.B.W. both agree to serve as corresponding authors for the work.

Competing interests

The authors have no competing interests to disclose.

have granted further insights into ECC by generating predictions that can inform future experimentation, and provided quantitative characterizations of events that are currently difficult (or impossible) to investigate experimentally (Smith *et al.* 1998; Sobie *et al.* 2002, 2006, 2017; Ramay *et al.* 2011; Williams *et al.* 2011; Wagner *et al.* 2012; Greiser *et al.* 2014; Walker *et al.* 2014; Brandenburg *et al.* 2016; Wescott *et al.* 2016).

Recent evidence implicates the mechanics of contraction as a regulator of cardiac ECC through mechano-chemo-transduction (MCT) signalling (see Fig. 1; Petroff *et al.* 2001; Niggli *et al.* 2013; Jian *et al.* 2014). While reactive nitrogen species (RNS) have been implicated as a MCT-generated signal regulating RyR2 and sarcolemmal stretch activated channels (SACs; i.e. TRPs), an early report showed that a brief diastolic stretch elicited $Ca^{2+}$ sparks independently of regulation by RNS or SACs (Iribe *et al.* 2009). Guided by our initial evidence that MCT through microtubules (MTs) drove $Ca^{2+}$ spark activation during diastolic stretch (Iribe *et al.* 2009) and earlier discoveries implicating MTs in regulating ECC in heart (Tsutsui *et al.* 1993; Tagawa *et al.* 1998), we focused our attention on the mechanisms by which MTs regulate $Ca^{2+}$ spark activation during stretch, seeking to add quantitative details to the pathway through a comprehensive computational model.

Taken together, our evidence shows that MCT through MTs activates NADPH oxidase 2 (NOX2)-derived reactive oxygen species (ROS), signals we termed X-ROS (Prosser *et al.* 2011). We showed MT-dependent MCT through X-ROS is encoded in the frequency (i.e. heart rate) and amplitude (i.e. preload) of stretch and that MTs stabilized by detyrosination, an enzymatic post-translational modification (PTM) of the $\alpha$-tubulin, governs this effect (Kerr *et al.* 2015). Importantly, our work in dystrophic cardiomyopathy links the disease-dependent increase in MT proliferation, level of detyrosination and NOX2 expression to the excess $Ca^{2+}$ spark activation linked to arrhythmia and disease progression. Consistent with the proximate role of MTs in the activation of X-ROS, targeting the disease-altered MT network (Kerr *et al.* 2015) is solely sufficient to abrogate the deleterious excess in stretch-activated $Ca^{2+}$ spark activity *in vitro* as well as workload-elicited $Ca^{2+}$-dependent arrhythmia *in vivo*.

Here, we have extended these discoveries and show that X-ROS sensitizes stretch activated channels (SACs), a result consistent with previous reports implicating ROS as regulators of SACs in healthy and diseased heart (Jung *et al.* 2008; Kerr *et al.* 2015). Informed by published work and the new results presented here, we have expanded upon and improved our existing computational models of cardiac ECC. These efforts have yielded a computational model integrating MT-dependent MCT and cardiomyocyte ECC through X-ROS. This new computational model is a powerful platform that lays the foundation for future investigations into MCT's influence on cardiac ECC under both physiological and pathological conditions.

## Methods

### Ethical approval

Animal care and procedures were approved and performed in accordance with the standards set forth by the University of Maryland, Baltimore, Institutional Animal Care and Use

Committee (Approval no. 0617015) and the *Guide for the Care and Use of Laboratory Animals* published by the US National Institutes of Health (NIH Publication, 8th edn, 2011). The study conformed to the principles and regulations of *The Journal of Physiology* (Grundy, 2015). WT (e.g. C57/B6) and MDX (D2.B10-Dmdmdx/J)) mice were purchased from The Jackson Laboratory (Bar Harbor, ME, USA). Of note, this dystrophin-deficient murine model on the DBA2 background presents with a more severe phenotype than seen in the MDX mice (C57BL/10ScSn-Dmdmdx/J) we profiled previously. All animals had access to food and water *ad libitum* and were exposed to a 12 h light-dark cycle. Mice were deeply anaesthetized with isoflurane anaesthesia (3%), delivered by a veterinary grade vaporizer. Euthanasia was by rapid exsanguination secondary to the removal of the heart.

## Cardiomyocyte isolation

Adult, male mice (8–16 weeks) were anaesthetized by isoflurane vapour, followed by the excision of the heart and enzymatic isolation of ventricular cardiomyocytes (VCMs) as previously described (Shioya, 2007). Cardiomyocytes were stored in a normal Tyrode solution containing (in mM): NaCl 140, KCl 5, $CaCl_2$ 1.8, $MgCl_2$ 0.5, HEPES 5, glucose 5, $NaH_2PO_4$ 0.33 (pH 7.4). Experiments were performed at room temperature (25°C).

## Immunostaining and western blot

Microtubule and sarcomere structure were profiled in cells fixed in paraformaldehyde (4%) for 15 min, followed by 10 min permeabilization with Triton X-100 (0.1%). SuperBlock™ phosphate-buffered saline (PBS) was used for blocking procedure and antibody dilution (Thermo Fisher Scientific, Waltham, MA, USA). The cells were incubated overnight (4°C) with mouse $\alpha$-tubulin antibody (Millipore Sigma, St Louis, MO, USA) and phalloidin conjugated with Alexa Fluor 633 (Thermo Fisher Scientific), followed by a 2 hour incubation in secondary anti-mouse antibody conjugated with Alexa Fluor 488 (Thermo Fisher Scientific). VCMs were imaged using a Nikon A1R inverted confocal microscope with a ×60/1.4 NA oil-immersion objective (Nikon, Melville, NY, USA).

The free and polymerized tubulin fractions were isolated from snap frozen hearts as in Belanto *et al.* (2016), with western blots for $\alpha$-tubulin and its detyrosinated form (i.e., glu-tubulin, the enzymatic removal of the C-terminal tyrosine yielding a terminal glutamate), as described (Kerr *et al.* 2015).

## Axial stretch of VCMs

All experiments were performed in custom-fabricated cell chambers mounted on an inverted microscope. The diastolic stretch was performed as previously described (Prosser *et al.* 2013b; Kerr *et al.* 2015). Briefly, glass cell holders (Ionoptix, Milton, MA, USA) were coated with a biological adhesive, MyoTak™ (Ionoptix). One glass cell holder was connected to a length controller (Nano-OP65, Mad City Labs, Madison, WI, USA) to control the stretch paradigms. Myocytes were attached at both ends by gently pressing down with the MyoTak-coated holder and then lifting the cell from the chamber bottom. Axial stretch was applied by movement of the length controller in response to variable voltage waveform controlled by software (Aurora Scientific, Ontario, Canada). Also, the sarcomere length was monitored with a high-speed video camera (Aurora Scientific). Average

sarcomere length prior to stretch was 1.8 μm. To assure proper attachment and stretch amplitude, the VCMs were subjected to stretch-relaxation trials before the experiments. Experimentation only proceeded with well-attached VCMs. Similar sarcomere length changes are achieved and maintained with static and 2 Hz cyclic (sinusoidal waveform) stretch (Prosser *et al.* 2011, 2013b; Kerr *et al.* 2015). Only cells with no signs of damage or disturbed integrity of cell membranes in response to any of the stretch paradigms were included in this study.

### $Ca^{2+}$ spark measurements

Cells were loaded with Fluo-4 by 15 min incubation with 3 μM of Fluo-4-acetoxymethyl (AM) ester (Thermo Fisher Scientific) and 0.01% Pluronic F127 (a poloxamer made by BASF, Florham Park, NJ, USA) followed by an additional 10 min for de-esterification. Cells were scanned using a 488 nm laser in a Nikon A1R inverted confocal microscope with a ×40/1.3 NA oil-immersion objective. The acquisition was performed in confocal line-scan mode at 1.84 ms per line. Automated analysis of line-scan images for $Ca^{2+}$ spark location and properties were performed using ImageJ (National Institutes of Health, Bethesda, MD, USA) with SparkMaster plugin (Picht *et al.* 2007).

### Manganese quench measurements

To determine the relative magnitude of $Ca^{2+}$ influx, we adopted and modified a ‘manganese (Mn) quench’ technique as we previously described (Kerr *et al.* 2015). In this method, the equimolar replacement of $Ca^{2+}$ with $Mn^{2+}$ in normal Tyrode solution results in $Mn^{2+}$ permeation through $Ca^{2+}$-permissive cation channels, which quenches the Fura-2 fluorescence ($E_x$: 360 nm, $E_m$: 510 nm). Here myocytes were loaded with 5 μM Fura-2 AM (Thermo Fisher Scientific) and 0.01% Pluronic F127 (see above) for 15 min followed by 10 min for de-esterification. Cells were imaged using an IX70 inverted fluorescence microscope (Olympus, Center Valley, PA, USA) with a ×40/1.1 NA water-immersion objective. The Fura-2 was excited at its isobestic point using a 360 nm light from the DG-4 illumination system (Sutter Instrument, Novato, CA, USA) and the emission was captured with a sCMOS camera (pco.edge 4.2, PCO AG, Kelheim, Germany) each second. Prior to stretch trial, the perfusion with normal Tyrode solution was switched to a Mn-Tyrode solution to establish the basal Mn permeability (30 s). Cells were then stretched for 60 s with a sinusoidal waveform (2 Hz; 10% cell length) as described previously (Prosser *et al.* 2011, 2013b; Kerr *et al.* 2015), followed by a return to resting sarcomere length (SL) (30 s). To evaluate the impact of ROS on the influx pathway, cells were incubated with normal Tyrode solution supplemented with 10 mM of *N*-acetyl L-cysteine (NAC; Millipore Sigma) for 5 min, followed by a second trial of $Mn^{2+}$ quenching and 2 Hz cyclic stretch.

### Statistics

All the data are presented as mean value ± standard error of the means (SEM) unless otherwise noted. Following a test for normality, either Student’s unpaired *t* test (for two groups) or one/two-way ANOVA (for more than two groups) was used for normally distributed data (Figs 2, 3 and 7). Data with a non-normal distribution was analysed with a Kruskal-Wallis one-way ANOVA within each genotype ($Ca^{2+}$ spark full width, half-maximum (FWHM), full duration, half maximum (FDHM) and amplitude, Fig. 4) or with

Friedman's repeated measures ANOVA across all groups ($Ca^{2+}$ spark frequency, Figs 4 and 6) with a corrected Bonferonni *post hoc* test for multiple comparisons (SigmaStat v 4.1 (Systat Software, Inc., San Jose, CA, USA) and SPSS Statistics v 26 (IBM Corp., Armonk, NY, USA)).

## Model formulation

The computational models of $Ca^{2+}$ signalling in heart utilized here are based on published work by our group (Williams *et al.* 2011; Walker *et al.* 2014; Wescott *et al.* 2016). The compartmental Monte Carlo model used here consists of ordinary differential equations (ODEs) representing the time-evolution of various intracellular ion concentrations (i.e. $[Ca^{2+}]_i$, $[Na^+]_i$, $[K^+]_i$,) and ion current gating variables. These ODEs are then coupled to two discrete-state, continuous-time Markov chains representing the stochastic gating of the LCC and RyR2. See Wescott *et al.* (2016) for more details. For the purposes of this study, the cell's sarcolemmal membrane was clamped to −80 mV to simulate a quiescent cardiomyocyte. The 3-D, spatial model of $Ca^{2+}$ diffusion utilized consists of four reaction-diffusion style, partial differential equations which govern the diffusion of free cytosolic $Ca^{2+}$, $Ca^{2+}$ bound to Fluo-4, free SR $Ca^{2+}$ and $Ca^{2+}$ bound to Fluo-5N over the simulated region. This spatial region was designed to mimic a transverse confocal linescan of a ventricular cardiomyocyte. Within this spatial domain, $Ca^{2+}$ release units (CRUs) are randomly distributed along the transverse direction with a mean inter-CRU distance of 0.6 $\mu$m. Details regarding channel gating were identical between the compartmental and spatial formulations. See Walker *et al.* (2014) and Wescott *et al.* (2016) for more details.

**Simplified X-ROS formulation—**Based on results from our group and others, we have focused modelling MT-dependent MCT via three primary components that activate during sarcomere stretch: (1) mechanical strain within MTs activates NOX2; (2) NOX2 generates X-ROS signals; and (3) X-ROS signals sensitize the activation of RyR2 and SACs (for review see Prosser *et al.* 2013a). We have delimited our model to address these components.

**Sarcomere length:** During stretch, current SL (SL) is governed by:

$$SL = SL_1 + A_s \sin(2\pi\omega t - \pi/2) \quad (1)$$

where $SL_1$ = 1.92 $\mu$m, and $A_s$ = 0.08 $\mu$m.

**NOX2 activity:** Here we present a discrete-state, continuous-time Markov chain designed to simulate the activity of NOX2 in heart. This Markov chain is represented by the following three-state transition-state diagram, where D represents the 'deactivated' state, A the 'activated' state, and R the 'refractory' state.

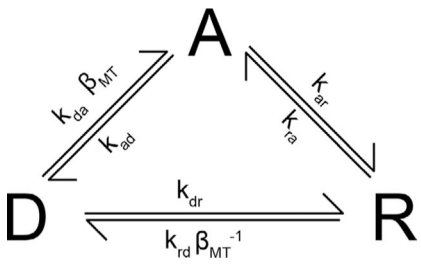


(2)

where each $k$ (e.g. $k_{da}$, $k_{ad}$, etc.) is a rate constant with units of $s^{-1}$ (see Table 1) and $\beta_{MT}$ is a unitless 'MT strain' factor for NOX2 given by:

$$\beta_{MT} = H[SL - SL_R]\left(\beta_m \frac{SL/SL_R - 1}{\beta_1}\right)^{\beta_\eta} + \beta_0 \quad (3)$$

where $H$ is the heaviside function, $SL_R$ is the resting sarcomere length, $\beta_m$ is a MT strain factor scalar, $\beta_n$ is MT strain cooperativity factor, $\beta_1$ is the maximal MT strain factor, and $\beta_0$ is the minimal MT strain factor (see Table 1).

**RyR2 sensitization by ROS:** Previously established RyR2 gating rate constants are scaled by an 'oxidization' factor ($\chi$) which is given by:

$$\chi = 1 + (\rho_X - \rho_X^o)\pi_X^A - \rho_X^o \quad (4)$$

where $\rho_X$ is an 'X-ROS scalar' formed by the relative densities of MTs and NOX2 ($\rho_{MT}$ and $\rho_{NOX2}$, respectively) such that $\rho_X = \rho_{MT}\rho_{NOX2}$, $\rho_X^o$ represents a basal oxidization factor, and $\pi_X^A$ is the probability of NOX2 being activated (in state 'A' from above). Each RyR2's gating is determined by the following two-state, continuous-time Markov chain represented by the following transition-state diagram,

$$\text{(Closed)} \quad \mathscr{C} \quad \underset{k_{21}/\chi^2}{\overset{\chi k_{12} c_{ds}^n \phi}{\rightleftharpoons}} \quad \mathscr{O} \quad \text{(Open)} \quad (5)$$

where $k_{12}$ is the basal RyR2 opening rate in $\mu M^{-\eta}\, s^{-1}$, $\Phi$ is a luminal regulation function (see Wescott *et al.* 2016), $c_{ds}$ is the subspace $[Ca^{2+}]$, $\eta$ is the RyR2 $Ca^{2+}$-binding cooperativity constant and $k_{21}$ is the intrinsic RyR2 closing rate in $s^{-1}$.

While simple and computationally efficient, this formulation accurately captures both the activation of NOX2 and how NOX2-produced ROS alters RyR2 gating during stretch across both static and cyclical stretch protocols (see Results).

**Stretch-dependent $Ca^{2+}$ influx in heart:** Evidence suggests that sarcolemmal stretch-activated channels (SACs; i.e. TRPs) contribute to the dynamic regulation of $Ca^{2+}$ in cardiomyocytes (Zeng *et al.* 2000; Kondratev *et al.* 2005; Aguettaz *et al.* 2016). A stretch-

activated $Ca^{2+}$ influx (SACa) current was added to the existing computational model and was constrained by $Ca^{2+}$ influx measurements shown here (see Fig. 4). This $Ca^{2+}$ current takes the following form:

$$I_{\text{saca}} = \frac{(\chi - 1)^2}{(\chi - 1)^2 + \left(K_{\text{d}}^{\chi}\right)^2} g_{\text{saca}}(V - E_{Ca}) \quad (6)$$

where $K_{\text{d}}^{\text{X}}$ is the sensitivity coefficient for activating $I_{\text{saca}}$, $g_{\text{saca}}$ is the whole conductance for the current, $V$ is the sarcolemmal membrane voltage (in mV), and $E_{\text{Ca}}$ is the Nernst reversal potential for $Ca^{2+}$.

## Results

Having established the formulation for our computational model, we next performed a focused series of experimental tests to expand our understanding of three main areas of stretch-dependent $Ca^{2+}$ signalling in the heart. First, we quantified the alterations in MT network associated with disease (i.e. MDX), then we characterized the amount of $Ca^{2+}$ that enters a VCM during stretch, and finally how $Ca^{2+}$ spark properties are altered during stretch in both healthy and diseased hearts. The computational model was constrained and simulations were performed to assess the ability of the model to make predictions regarding MT-driven changes in $Ca^{2+}$ signalling.

### MT density, levels of detyrosination and NOX2 expression are increased in disease

We have previously linked both the increase in MT densification and its stabilization by detyrosination as well as the increased NOX2 expression, to the increased X-ROS generation in the dystrophic heart (Kerr *et al.* 2015). Here we have characterized and quantified the changes in MTs and NOX2 and used the results to improve our computational model of X-ROS. VCMs from WT and MDX mice were immunolabelled with antibodies (Abs) against $\alpha$-tubulin (Fig. 2A and B) and phalloidin to visualize actin (not shown). We showed MDX VCMs have an ~50% increase in MT density compared to WT (Fig. 2C), confirmed by western blot quantification of the polymerized MT fraction from intact hearts, which showed a 1.5-fold increase in polymerized MT fraction, confirming this finding. Free tubulin was also increased in the dystrophic hearts, consistent with an increase in tubulin expression further contributing to this effect. Additionally, there was a proportional increase in glu-tubulin in the polymerized MT fraction, which we have shown is essential to MT-dependent MCT (Kerr *et al.* 2015)). Together, these changes are qualitatively similar to those we have previously shown in hearts from aged MDX mice. Western blot quantification of WT *vs.* MDX also revealed an ~2.5-fold increase in gp91phox, the catalytic subunit of NOX2. Again, this increase was similar to our previous work in the aged MDX (Kerr *et al.* 2015).

### Stretch-activated $Ca^{2+}$ influx

We adopted a modified manganese ($Mn^{2+}$) quench technique to assess the magnitude of $Ca^{2+}$ influx in Fura-2-loaded VCMs both at rest and with stretch imposed by our single myocyte stretch device (see Methods). Before stretch, each cardiomyocyte was adjusted to a

consistent SL of (1.84 $\mu$m). Immediately upon application of $Mn^{2+}$ containing perfusate, cation influx was observed via quenching of Fura-2 (see Slope 1 of Fig. 3A). Upon initiation of a cyclical stretch protocol (2 Hz sinusoidal with amplitude of 10% of SL for 2 min), there was a significant increase in $Mn^{2+}$ quench rate (see SL plot in Fig. 5A), as we previously described in skeletal muscle (Kerr *et al.* 2015). These results suggest that in the heart, physiological stretch elicits an ~2-fold increase of $Ca^{2+}$ entry over basal conditions. Note that while basal $Ca^{2+}$ entry is relatively small (~1 $\mu M\ s^{-1}$, see Trafford *et al.* 1997), this 2-fold change in influx will critically alter steady-state $Ca^{2+}$ homeostasis. Finally, given that the majority of the stretch-dependent cation influx was attenuated by scavenging ROS with NAC, we conclude that stretch-dependent ROS is a potent regulator of SAC activity during stretch. This ability of ROS to regulate $I_{saca}$ is reflected in Eqn (6).

## Stretch-dependent changes in $Ca^{2+}$ sparks

We previously established that $Ca^{2+}$ spark frequency was exquisitely sensitive to stretch via MTs and X-ROS; however, the impact on spark properties was not evaluated. Here we used a single static stretch and confocal linescan recording to profile $Ca^{2+}$ sparks in both WT (Fig. 4A) and MDX (Fig. 4B) VCMs. Upon stretch (red arrow) we observed a rapid increase in $Ca^{2+}$ spark frequency consistent with our previous work in MDX mice (see Prosser *et al.* 2011). Expanding upon our other work (Prosser *et al.* 2011, 2013b; Kerr *et al.* 2015), we now show that while the amplitude ($\Delta F/F_O$) and spatial extent (full width, half-maximum; FWHM) of $Ca^{2+}$ sparks are insensitive to stretch, the temporal extent (full duration, half maximum; FDHM) is significantly increased (see Fig. 4C). Taken together, these results provide critical details regarding the overall amount of SR $Ca^{2+}$ release during stretch and aided in constraining the computational model.

## Modelling stretch-dependent RyR2 activation in heart

Our approach to modelling stretch-dependent changes in $Ca^{2+}$ signalling in heart began with our representation of NOX2 activation. Our imaging of stretch-dependent ROS (via fluorescence of $H_2$-dichlorofluorescein) demonstrated that the rate of X-ROS generation is maximal immediately upon stretch and rapidly decays with either the immediate return to resting length or if the stretch is maintained (Prosser *et al.* 2011). In contrast, a cyclic stretch protocol sustains the generation of X-ROS (Prosser *et al.* 2013b). To approximate this behaviour in our model we utilized a Markov chain representation of NOX2 (see Eqn (2)). Here the mechanical stress of stretch imparts a strain in the MTs ($\beta_{MT}$) that activates NOX2 to initiate a burst of ROS. If the stretch is sustained (Fig. 5A, SL, blue), NOX2 transitions into a refractory state (state R in Eqn (2)), which reduces the rate of NOX2 activity (i.e. ROS production) (Fig. 5B, blue). During a cyclical stretch perturbation (Fig. 5A, SL, red), releasing strain on the MT network allows NOX2 to recover from the refractory state (R) to the deactivated state (state D in Eqn (2)) and become available for reactivation by a subsequent stretch. The model behaviour across either sustained or cyclic stretch (Fig. 5A), or with varying amplitudes of stretch (Fig. 5B), faithfully captures the experimental behaviour that we previously observed (Prosser *et al.* 2013b).

Having established the model parameters for NOX2 activity (i.e. X-ROS), this behaviour was translated into a change in RyR2 gating (via $\chi$, see Eqn (4) and Fig. 5A) where both the

opening and closing rates of RyR2 ($k_{12}$ and $k_{21}$ in Eqn (5), respectively) are modified (see Eqn (5)) in a manner consistent with observed changes in RyR2 gating following oxidation of RyR2 by $H_2O_2$ (Boraso & Williams, 1994). This redox-dependent RyR2 gating results in a slight increase RyR2 $P_O$ during stretch (see Fig. 5A), which in turn drives a change in $Ca^{2+}$ spark behaviour with sustained (Fig. 5C) or cyclic stretch (Fig. 5D). While these results are consistent with our published experimental observations (Prosser *et al.* 2013b), a closer examination revealed two notable findings.

First, our analysis of both model- and experiment-derived sparks showed that the model also identified FDHM as a spark parameter sensitive to stretch (Figs 4C and 5B). Second, while our brief cyclic stretch (10 s, Fig. 5D) yielded a sustained $Ca^{2+}$ spark activity as in our previous work (Prosser *et al.*, 2013b), the rapid cessation of $Ca^{2+}$ spark activity upon return to rest did not align with the latency of spark cessation seen in this previous experimental work. To investigate this discrepancy, we extended our model simulation to 60 s of cyclic stretch and observed a 2-fold increase in spark frequency for at least 10 s into the post-stretch period (not shown).

## Modelling captures deleterious $Ca^{2+}$ release in Duchenne muscular dystrophy

A major pathological sequelae of Duchenne muscular dystrophy (DMD) is cardiomyopathy and arrhythmia. In the *mdx* model of murine DMD, we linked the disease-dependent increase in MT density, the abundance of glu-tubulin and increased NOX2 expression to the deleterious increase in $Ca^{2+}$ sparks and arrhythmogenic $Ca^{2+}$ waves. As an empirical test of our model we sought to account for this behaviour by altering model parameters *a priori* based on our published and new experimental results.

Our work established MTs as central to the activation of NOX2 by MCT and showed that the abundance of glu-tubulin is critical to this effect. Recent elegant work in cardiomyocytes demonstrated that the level of glu-tubulin determines how MTs buckle under and bear the mechanical stress which transmits mechanical strain to regulate MCT (Robison *et al.* 2016). Given that we identified a ~50% increase in MT density in MDX (immunohistochemistry and western blot, see Fig. 2) with a proportionate increase in glu-tubulin, and a ~150% increase in NOX2 content, we implemented a scale factor for changes in MT and NOX2 density in MDX *vs.* WT (see Table 2, $\rho_{MT} = 1.5$ and $\rho_{NOX2} = 2.5$, respectively) in our model as conservative estimates for their influence on X-ROS in MDX. We also included alterations in SERCA and NCX activity associated with MDX animals (see Table 2; Fauconnier *et al.* 2010; Wang *et al.* 2015).

We show the influence of static and cyclic stretch on $Ca^{2+}$ spark activity in simulated transverse, confocal linescans from WT VCMs and see this behaviour dramatically increased in MDX (Fig. 6). In fact, cyclic stretch generates $Ca^{2+}$ release activity that transitions from stable $Ca^{2+}$ sparks to elevated levels of pro-arrhythmic $Ca^{2+}$ release. This behaviour is reflected in the RyR2 integrated flux that underscores this behaviour, a behaviour driven by the model elements that impose a MT-dependent X-ROS signal that drives an increase in SAC dependent $Ca^{2+}$ influx as well as an increase in RyR2 activation from CICR as well as luminal-dependent mechanisms (see Walker *et al.* 2014; Wescott *et al.* 2016).

### Targeting the MT network effectively suppresses $Ca^{2+}$-dependent arrhythmias

Our evidence that targeting either MT density or its level of glu-tubulin was solely sufficient to abrogate the deleterious excess in stretch-activated X-ROS and $Ca^{2+}$ spark activity *in vitro*, and workload elicited $Ca^{2+}$-dependent arrhythmia *in vivo*, was firm evidence that MTs were central to disease pathology in DMD. Consistent with these published reports, our model simulations show that the normalization of MT-dependent MCT through X-ROS effectively suppressed the dysregulated excess of stretch-dependent $Ca^{2+}$ spark activity and arrhythmogenic $Ca^{2+}$ release in the MDX (see Figs 6C and 7).

## Discussion

We have presented a new computational model of X-ROS that tightly integrates the MT-dependent activation of NOX2 with stretch-dependent changes in $Ca^{2+}$ signalling in heart. This model was directly informed by quantitative experimental measures and accurately captured our current and prior experimental findings that diastolic stretch elicits NOX2-dependent ROS signals which regulate $Ca^{2+}$ sparks and cardiac ECC. Given the diverse roles played by MTs in cell physiology, our ability to account for our experimental observations with a computational model constrained by the biophysical aspects of MCT and independent of the effects of MTs on other pathways adds critical support to our hypothesis that MTs act primarily via MCT and NOX2 to regulate $Ca^{2+}$ signalling in heart.

Notably, only a modest number of model parameters and disease-relevant scaling factors were sufficient to account for the influence of MCT through X-ROS in the healthy and diseased heart. While the ability of our computational models to faithfully account for this MCT regulation of cardiac ECC while utilizing a small number of factors is exciting, the underlying regulatory complexity within each factor prompts several questions based on this and other findings. For example, in the model, MT strain (i.e. $\beta_{MT}$) is responsible for translating the mechanical energy of stretch to activate NOX2. However, within the cell, MT strain is determined by glu-tubulin-enriched MTs in concert with intermediate filaments (IF) and other cytolinker proteins, which also exhibit increased expression in disease. Furthermore, evidence suggests that MT and other cytoskeletal changes regulate the mechanical properties (i.e. stiffness) of the cytoskeleton to regulate MCT (Kerr *et al.* 2015; Robison *et al.* 2016). In this regard, future experimental and computational efforts directed towards understanding how cytoskeletal elements act together or separately to regulate X-ROS and how measured changes in cytoskeletal mechanics relate to the magnitude of X-ROS will greatly advance our understanding.

Our published work (Kerr *et al.* 2015) combined with new results from experiments and computational modelling provides clear evidence that MTs are essential for the activation of NOX2 via MCT. While our implementation of a three-state Markov chain faithfully captures how MT strain drives the complex behaviour of the experimentally observed X-ROS signals, whether MTs activate NOX2 by a direct mechanical means or via a MCT elicited effect (see Allen *et al.* 2016) remains unanswered.

Our experiments, and computational model, also revealed MCT through X-ROS as a regulator of mechano-sensitive sarcolemmal $Ca^{2+}$ influx in the heathy heart and showed

increased MCT through X-ROS underscores its excess in disease (Kerr *et al.* 2015). These findings add to the evidence implicating NOX2-ROS for the dysregulated sarcolemmal influx in the dystrophic heart (Gonzalez *et al.* 2014). Additionally, while MT-dependent MCT via X-ROS appears to be the dominant signal elicited by stretch, evidence from others shows that MCT-dependent RNS signals (i.e. NO) contribute to RyR2 (Petroff *et al.* 2001; Jung *et al.* 2008; Shkryl *et al.* 2009; Niggli *et al.* 2013; Jian *et al.* 2014) and TRP channel (Koitabashi *et al.* 2010; Seo *et al.* 2014a,b) regulation in heart. Whether MCT-dependent X-ROS and RNS interact independently or synergistically to RyR2 or TRPs is another unanswered question. One possible interaction is sustained $Ca^{2+}$ spark activity observed after the cyclic stretch (Prosser *et al.* 2013b). While our simulation shows the accompanying elevation in $[Ca^{2+}]_i$ (by ~20 nM) and SR $Ca^{2+}$ (by ~50 $\mu$M) was a parsimonious explanation for the sustained level of spark activity seen here, we remain intrigued that this level of $Ca^{2+}$ could also activate nNOS-dependent NO signals (Jian *et al.* 2014) that could further sustain this spark activity in this post-stretch period.

In summary, we presented a new computational model integrating MT-dependent MCT and cardiomyocyte ECC through X-ROS. In conjunction with advanced *in vitro* approaches as shown here (see Methods), this model is a powerful platform that lays the foundation for future investigations into the influence of MCT on cardiac ECC under both physiological and pathological conditions.

## Funding

This work was partially supported by NIH grants; R01 AR071618 (C.W.W.) and K25 HL125762 (G.S.B.W.).

## Biography

**Humberto Joca** obtained his Master's degree in Physiology at the State University of Ceará (Brazil) and his PhD at the Federal University of Minas Gerais (Brazil). Humberto currently is a postdoctoral researcher at University of Maryland School of Medicine, with a focus on understanding the mechanotransduction in muscle cells and its role in excitation-contraction coupling. He is also interested in a wide range of experimental techniques, such as patch-clamp electrophysiology, *in vitro* force measurements, super-resolution and confocal microscopy, and image/signal processing.

## References

Aguettaz E, Lopez JJ, Krzesiak A, Lipskaia L, Adnot S, Hajjar RJ, Cognard C, Constantin B & Sebille S (2016). Axial stretch-dependent cation entry in dystrophic cardiomyopathy: Involvement of several TRPs channels. Cell Calcium 59, 145–155. [PubMed: 26803937]

Allen DG, Whitehead NP & Froehner SC (2016). Absence of dystrophin disrupts skeletal muscle signaling: Roles of $Ca^{2+}$, reactive oxygen species, and nitric oxide in the development of muscular dystrophy. Physiol Rev 96, 253–305. [PubMed: 26676145]

Belanto JJ, Olthoff JT, Mader TL, Chamberlain CM, Nelson DM, McCourt PM, Talsness DM, Gundersen GG, Lowe DA & Ervasti JM (2016). Independent variability of microtubule perturbations associated with dystrophinopathy. Hum Mol Genet 25, 4951–4961. [PubMed: 28171583]

Boraso A & Williams AJ (1994). Modification of the gating of the cardiac sarcoplasmic reticulum $Ca^{2+}$-release channel by $H_2O_2$ and dithiothreitol. Am J Physiol 267, H1010–H1016. [PubMed: 8092267]

Brandenburg S, Kohl T, Williams GS, Gusev K, Wagner E, Rog-Zielinska EA, Hebisch E, Dura M, Didie M, Gotthardt M, Nikolaev VO, Hasenfuss G, Kohl P, Ward CW, Lederer WJ & Lehnart SE. (2016) Axial tubule junctions control rapid calcium signaling in atria. J Clin Invest 126, 3999–4015. [PubMed: 27643434]

Cheng H & Lederer WJ (2008). Calcium sparks. Physiol Rev 88, 1491–1545. [PubMed: 18923188]

Cheng H, Lederer WJ & Cannell MB (1993). Calcium sparks: elementary events underlying excitation-contraction coupling in heart muscle. Science 262, 740–744. [PubMed: 8235594]

Fauconnier J, Thireau J, Reiken S, Cassan C, Richard S, Matecki S, Marks AR & Lacampagne A. (2010) Leaky RyR2 trigger ventricular arrhythmias in Duchenne muscular dystrophy. Proc Natl Acad Sci U S A 107, 1559–1564. [PubMed: 20080623]

Gonzalez DR, Treuer AV, Lamirault G, Mayo V, Cao Y, Dulce RA & Hare JM (2014). NADPH oxidase-2 inhibition restores contractility and intracellular calcium handling and reduces arrhythmogenicity in dystrophic cardiomyopathy. Am J Physiol Heart Circ Physiol 307, H710–H721. [PubMed: 25015966]

Greiser M, Kerfant BG, Williams GS, Voigt N, Harks E, Dibb KM, Giese A, Meszaros J, Verheule S, Ravens U, Allessie MA, Gammie JS, van der Velden J, Lederer WJ, Dobrev D & Schotten U (2014) Tachycardia-induced silencing of subcellular $Ca^{2+}$ signaling in atrial myocytes. J Clin Invest 124, 4759–4772. [PubMed: 25329692]

Grundy D (2015). Principles and standards for reporting animal experiments in *The Journal of Physiology* and *Experimental Physiology*. Exp Physiol 100, 755–758. [PubMed: 26076765]

Iribe G, Ward CW, Camelliti P, Bollensdorff C, Mason F, Burton RA, Garny A, Morphew MK, Hoenger A, Lederer WJ & Kohl P (2009). Axial stretch of rat single ventricular cardiomyocytes causes an acute and transient increase in $Ca^{2+}$ spark rate. Circ Res 104, 787–795. [PubMed: 19197074]

Jian Z, Han H, Zhang T, Puglisi J, Izu LT, Shaw JA, Onofiok E, Erickson JR, Chen YJ, Horvath B, Shimkunas R, Xiao W, Li Y, Pan T, Chan J, Banyasz T, Tardiff JC, Chiamvimonvat N, Bers DM, Lam KS & Chen-Izu Y (2014). Mechanochemotransduction during cardiomyocyte contraction is mediated by localized nitric oxide signaling. Sci Signal 7, ra27. [PubMed: 24643800]

Jung C, Martins AS, Niggli E & Shirokova N (2008). Dystrophic cardiomyopathy: amplification of cellular damage by $Ca^{2+}$ signalling and reactive oxygen species-generating pathways. Cardiovasc Res 77, 766–773. [PubMed: 18056762]

Kerr JP, Robison P, Shi G, Bogush AI, Kempema AM, Hexum JK, Becerra N, Harki DA, Martin SS, Raiteri R, Prosser BL & Ward CW (2015). Detyrosinated microtubules modulate mechanotransduction in heart and skeletal muscle. Nat Commun 6, 8526. [PubMed: 26446751]

Koitabashi N, Aiba T, Hesketh GG, Rowell J, Zhang M, Takimoto E, Tomaselli GF & Kass DA (2010). Cyclic GMP/PKG-dependent inhibition of TRPC6 channel activity and expression negatively regulates cardiomyocyte NFAT activation: Novel mechanism of cardiac stress modulation by PDE5 inhibition. J Mol Cell Cardiol 48, 713–724. [PubMed: 19961855]

Kondratev D, Christ A & Gallitelli MF (2005). Inhibition of the $Na^{+}$-$H^{+}$ exchanger with cariporide abolishes stretch-induced calcium but not sodium accumulation in mouse ventricular myocytes. Cell Calcium 37, 69–80. [PubMed: 15541465]

Niggli E, Ullrich ND, Gutierrez D, Kyrychenko S, Polakova E & Shirokova N (2013). Posttranslational modifications of cardiac ryanodine receptors: $Ca^{2+}$ signaling and EC-coupling. Biochim Biophys Acta 1833, 866–875. [PubMed: 22960642]

Petroff MG, Kim SH, Pepe S, Dessy C, Marban E, Balligand JL & Sollott SJ (2001). Endogenous nitric oxide mechanisms mediate the stretch dependence of $Ca^{2+}$ release in cardiomyocytes. Nat Cell Biol 3, 867–873. [PubMed: 11584267]

Picht E, Zima AV, Blatter LA & Bers DM (2007). SparkMaster: automated calcium spark analysis with ImageJ. Am J Physiol Cell Physiol 293, C1073–C1081. [PubMed: 17376815]

Prosser BL, Khairallah RJ, Ziman AP, Ward CW & Lederer WJ (2013a). X-ROS signaling in the heart and skeletal muscle: stretch-dependent local ROS regulates $[Ca^{2+}]_i$. J Mol Cell Cardiol 58, 172–181. [PubMed: 23220288]

Prosser BL, Ward CW & Lederer WJ (2011). X-ROS signaling: rapid mechano-chemo transduction in heart. Science 333, 1440–1445. [PubMed: 21903813]

Prosser BL, Ward CW & Lederer WJ (2013b). X-ROS signalling is enhanced and graded by cyclic cardiomyocyte stretch. Cardiovasc Res 98, 307–314. [PubMed: 23524301]

Ramay HR, Liu OZ & Sobie EA (2011). Recovery of cardiac calcium release is controlled by sarcoplasmic reticulum refilling and ryanodine receptor sensitivity. Cardiovasc Res 91, 598–605. [PubMed: 21613275]

Robison P, Caporizzo MA, Ahmadzadeh H, Bogush AI, Chen CY, Margulies KB, Shenoy VB & Prosser BL (2016). Detyrosinated microtubules buckle and bear load in contracting cardiomyocytes. Science 352, aaf0659. [PubMed: 27102488]

Seo K, Rainer PP, Lee DI, Hao S, Bedja D, Birnbaumer L, Cingolani OH & Kass DA (2014a). Hyperactive adverse mechanical stress responses in dystrophic heart are coupled to transient receptor potential canonical 6 and blocked by cGMP-protein kinase G modulation. Circ Res 114, 823–832. [PubMed: 24449818]

Seo K, Rainer PP, Shalkey Hahn V, Lee DI, Jo SH, Andersen A, Liu T, Xu X, Willette RN, Lepore JJ, Marino JP Jr, Birnbaumer L, Schnackenberg CG & Kass DA (2014b). Combined TRPC3 and TRPC6 blockade by selective small-molecule or genetic deletion inhibits pathological cardiac hypertrophy. Proc Natl Acad Sci U S A 111, 1551–1556. [PubMed: 24453217]

Shioya T (2007). A simple technique for isolating healthy heart cells from mouse models. J Physiol Sci 57, 327–335. [PubMed: 17980092]

Shkryl VM, Martins AS, Ullrich ND, Nowycky MC, Niggli E & Shirokova N (2009). Reciprocal amplification of ROS and $Ca^{2+}$ signals in stressed mdx dystrophic skeletal muscle fibres. Pflugers Arch 458, 915–928. [PubMed: 19387681]

Smith GD, Keizer JE, Stern MD, Lederer WJ & Cheng H (1998). A simple numerical model of calcium spark formation and detection in cardiac myocytes. Biophys J 75, 15–32. [PubMed: 9649364]

Sobie EA, Dilly KW, dos Santos Cruz J, Lederer WJ & Jafri MS (2002). Termination of cardiac $Ca^{2+}$ sparks: an investigative mathematical model of calcium-induced calcium release. Biophys J 83, 59–78. [PubMed: 12080100]

Sobie EA, Guatimosim S, Gomez-Viquez L, Song LS, Hartmann H, Saleet Jafri M & Lederer WJ (2006). The $Ca^{2+}$ leak paradox and rogue ryanodine receptors: SR $Ca^{2+}$ efflux theory and practice. Prog Biophys Mol Biol 90, 172–185. [PubMed: 16326215]

Sobie EA, Williams GSB & Lederer WJ (2017). Ambiguous interactions between diastolic and SR $Ca^{2+}$ in the regulation of cardiac $Ca^{2+}$ release. J Gen Physiol 149, 847–855. [PubMed: 28798276]

Tagawa H, Koide M, Sato H, Zile MR, Carabello BA & Cooper Gt (1998). Cytoskeletal role in the transition from compensated to decompensated hypertrophy during adult canine left ventricular pressure overloading. Circ Res 82, 751–761. [PubMed: 9562434]

Trafford AW, Diaz ME, Negretti N & Eisner DA (1997). Enhanced $Ca^{2+}$ current and decreased $Ca^{2+}$ efflux restore sarcoplasmic reticulum $Ca^{2+}$ content after depletion. Circ Res 81, 477–484. [PubMed: 9314828]

Tsutsui H, Ishihara K & Cooper Gt (1993). Cytoskeletal role in the contractile dysfunction of hypertrophied myocardium. Science 260, 682–687. [PubMed: 8097594]

Wagner E, Lauterbach MA, Kohl T, Westphal V, Williams GS, Steinbrecher JH, Streich JH, Korff B, Tuan HT, Hagen B, Luther S, Hasenfuss G, Parlitz U, Jafri MS, Hell SW, Lederer WJ & Lehnart SE (2012). Stimulated emission depletion live-cell super-resolution imaging shows proliferative

remodeling of T-tubule membrane structures after myocardial infarction. Circ Res 111, 402–414. [PubMed: 22723297]

Walker MA, Williams GS, Kohl T, Lehnart SE, Jafri MS, Greenstein JL, Lederer WJ & Winslow RL (2014). Superresolution modeling of calcium release in the heart. Biophys J 107, 3018–3029. [PubMed: 25517166]

Wang Q, Wang W, Wang G, Rodney GG & Wehrens XH (2015). Crosstalk between RyR2 oxidation and phosphorylation contributes to cardiac dysfunction in mice with Duchenne muscular dystrophy. J Mol Cell Cardiol 89, 177–184. [PubMed: 26555638]

Wescott AP, Jafri MS, Lederer WJ & Williams GS (2016). Ryanodine receptor sensitivity governs the stability and synchrony of local calcium release during cardiac excitation-contraction coupling. J Mol Cell Cardiol 92, 82–92. [PubMed: 26827896]

Williams GS, Chikando AC, Tuan HT, Sobie EA, Lederer WJ & Jafri MS (2011). Dynamics of calcium sparks and calcium leak in the heart. Biophys J 101, 1287–1296. [PubMed: 21943409]

Zeng T, Bett GC & Sachs F (2000). Stretch-activated whole cell currents in adult rat cardiac myocytes. Am J Physiol Heart Circ Physiol 278, H548–H557. [PubMed: 10666087]

**Key points**

- Our group previously discovered and characterized the microtubule mechanotransduction pathway linking diastolic stretch to NADPH oxidase 2-derived reactive oxygen species signals that regulate calcium sparks and calcium influx pathways.
- Here we used focused experimental tests to constrain and expand our existing computational models of calcium signalling in heart.
- Mechanistic and quantitative modelling revealed new insights in disease including: changes in microtubule network density and properties, elevated NOX2 expression, altered calcium release dynamics, how NADPH oxidase 2 is activated by and responds to stretch, and finally the degree to which normalizing mechano-activated reactive oxygen species signals can prevent calcium-dependent arrhythmias.

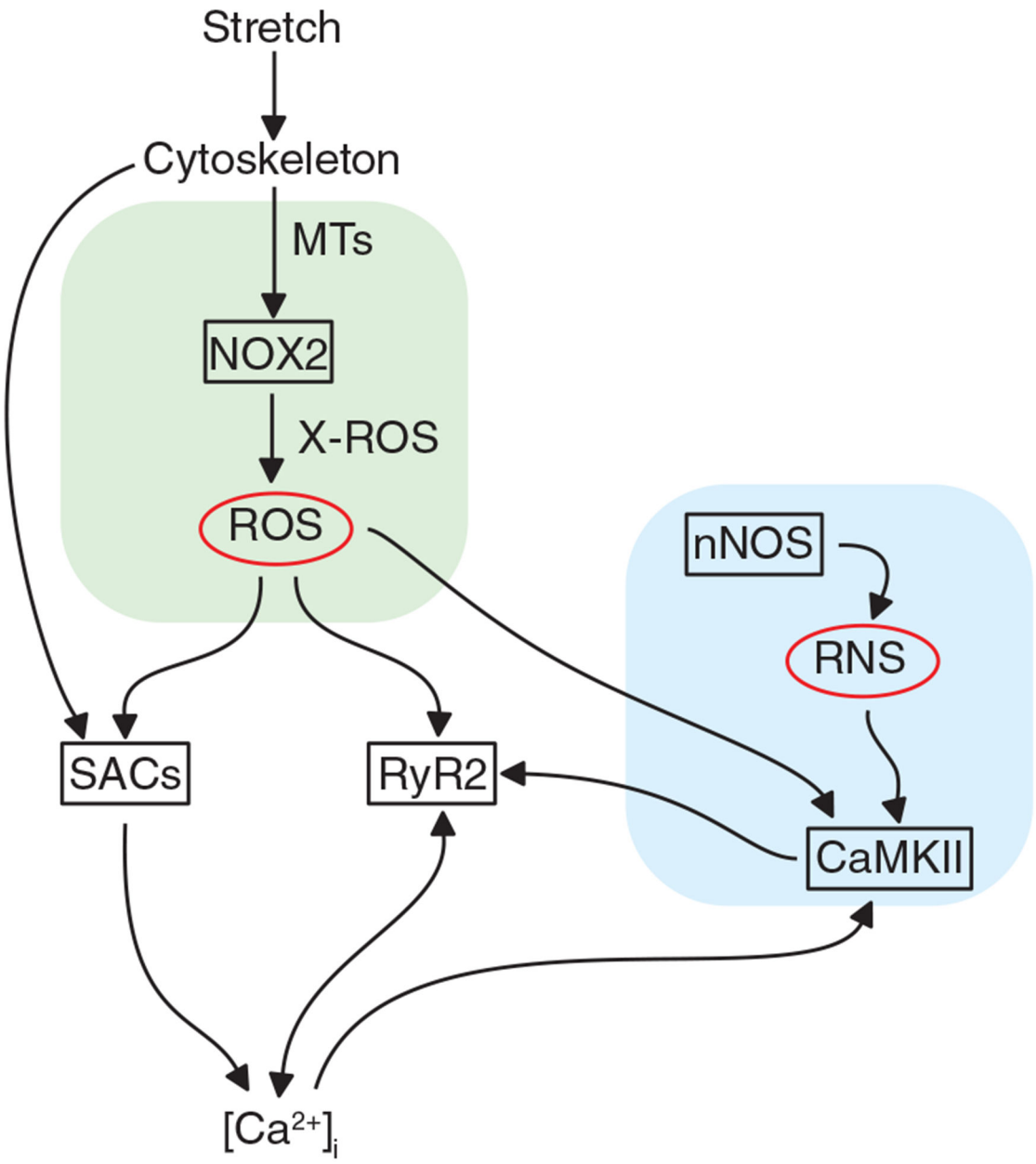


**Figure 1. Simplified diagram of stretch-dependent $Ca^{2+}$ signalling in heart**

$[Ca^{2+}]_i$, cytosolic $[Ca^{2+}]$; CaMKII, $Ca^{2+}$/calmodulin-dependent protein kinase II; MT, microtubule; nNOS, neuronal nitric oxide synthase; NOX2, NADPH oxidase 2; RNS, reactive nitrogen species; ROS, reactive oxygen species; RyR2, ryanodine receptor, type 2 SAC, stretch-activated channel.

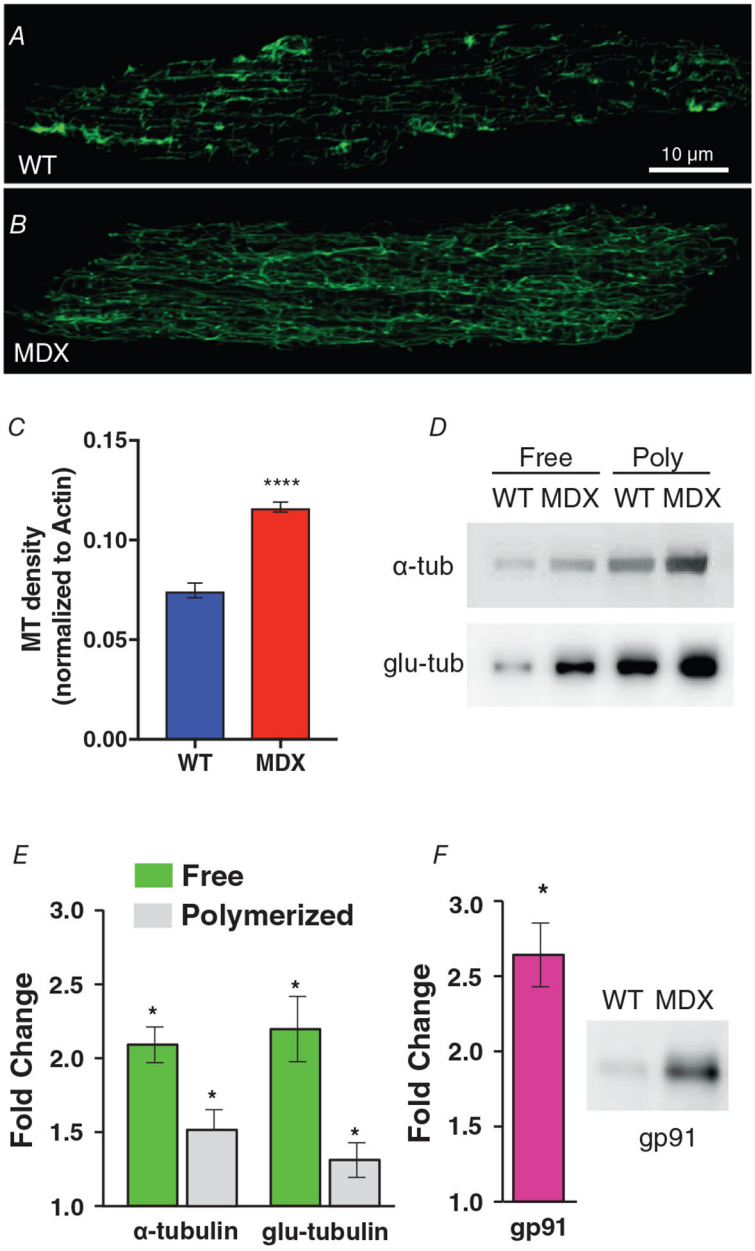


**Figure 2. Microtubules in heart**

*A* and *B*, VCMs from WT (*A*) and MDX (*B*) hearts immunolabelled for α-tubulin. *C*, quantification of MT density was obtained by normalizing the skeletonized binary area of α-tubulin (*A* and *B*) over the binary area of actin (not shown). *D*, western blots for free and polymerized fraction of a-tubulin and glu-tubulin, respectively. *E*, quantification of western blot in MDX hearts showing the overexpression of tubulin proteins over WT hearts. *F*, western blots and quantification (fold change) for total gp91 expression in WT and MDX. **** $P < 0.001$, * $P < 0.05$ over WT group.

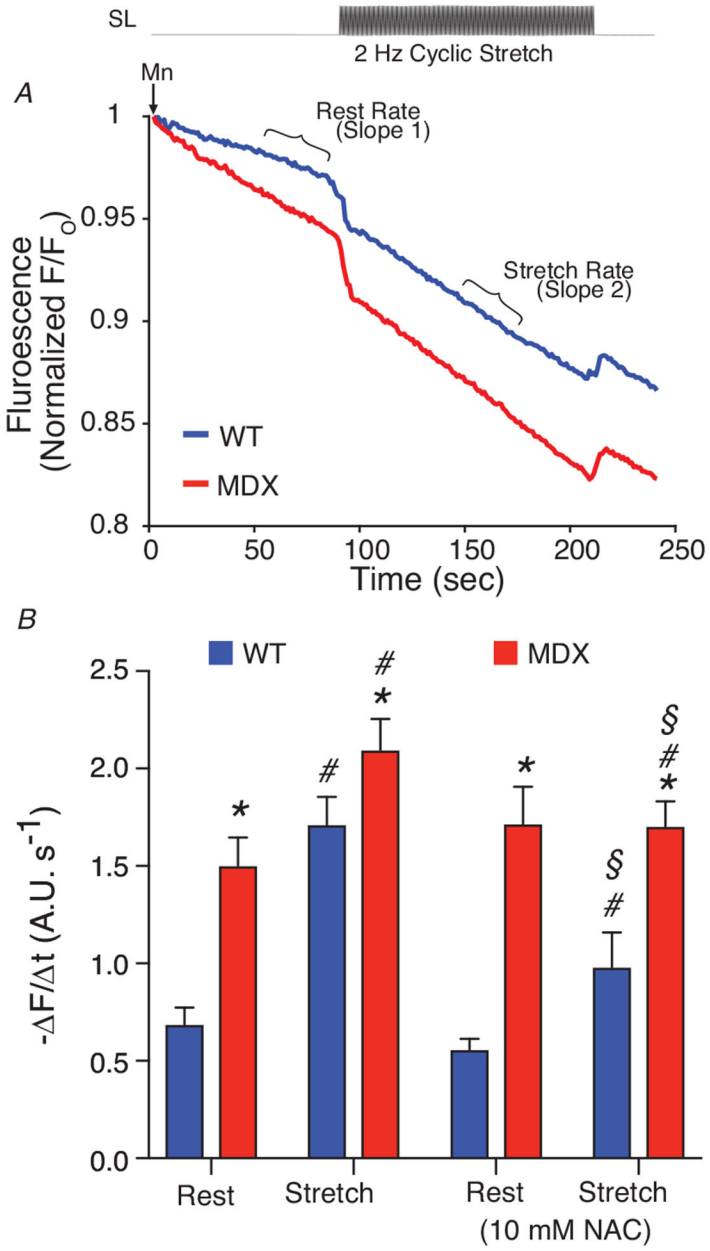


**Figure 3. Physiological stretch alters $Ca^{2+}$ entry in heart**

VCMs are first attached to glass cardiac fingers (see Methods). VCMs are loaded with Fura-2 AM (5 $\mu$M, 15 min). *A*, extracellular $Ca^{2+}$ (1.8 mM) is replaced with equimolar $Mn^{2+}$ which enters the cell via sarcolemmal $Ca^{2+}$ channels and quenches Fura-2 florescence (see Slope 1). During a 2 Hz cyclic stretch, elevated $Ca^{2+}$ influx increases the quench rate (see Slope 2). *B*, analysis of $Ca^{2+}$ influx rates. Statistics: MDX compared to WT ($^{*}P < 0.05$), Stretch compared to Rest ($^{\#}P < 0.05$), and NAC compared to vehicle ($^{\S}P < 0.05$).

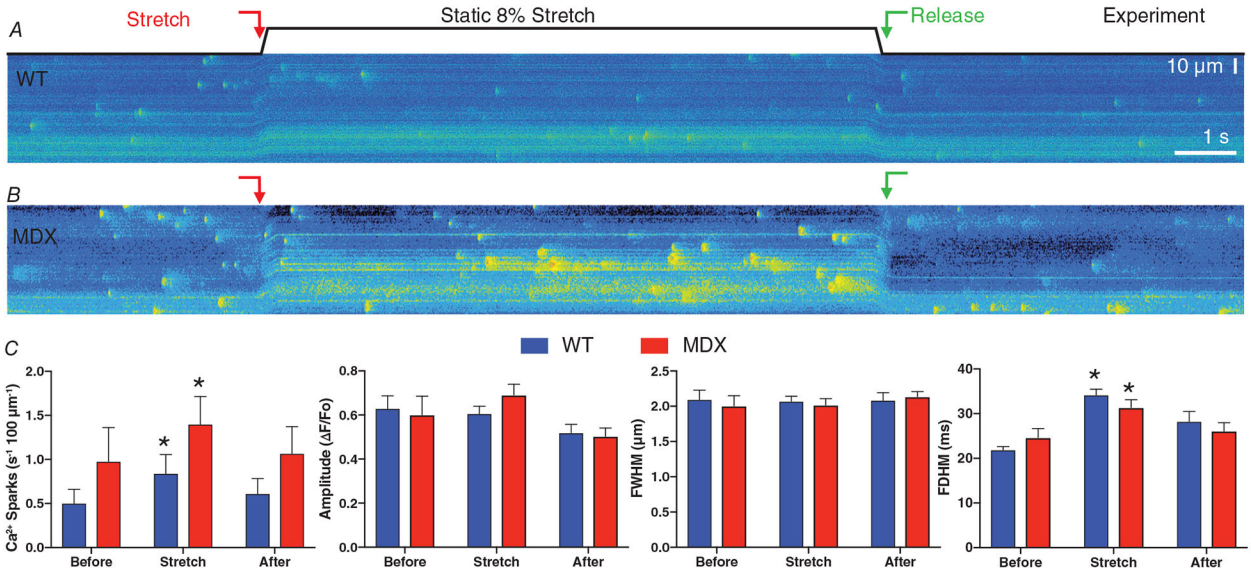


**Figure 4. Stretch-dependent changes in $Ca^{2+}$ signalling in heart**

*A* and *B*, representative, longitudinal confocal linescans for WT (*A*) and MDX (*B*) VCMs loaded with Fluo-4 AM. *C*, $Ca^{2+}$ spark frequency, amplitude, FDHM and FWHM before, during and after a static, 8% stretch. Statistics: Stretch compared to Before (*$P < 0.05$).

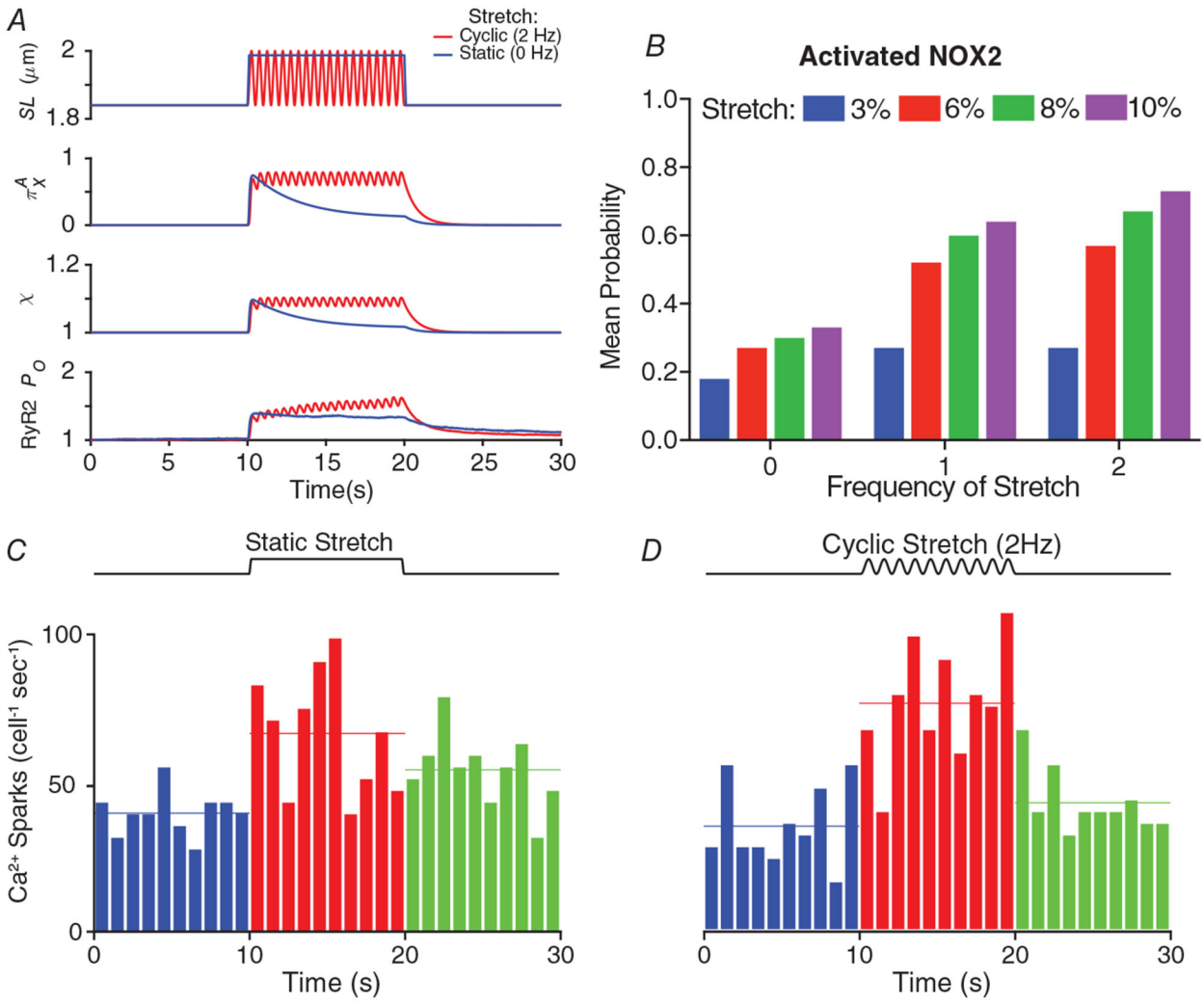


**Figure 5. Simulating stretch-dependent changes in $Ca^{2+}$ signalling in heart**

*A*, sarcomere length during a static (0 Hz, blue) and cyclical (2 Hz, red) stretch protocol, the instantaneous probability of NOX2 being in the activated state ($\pi_X^A$, see Eqn (2)), X-ROS factor ($\chi$), and the instantaneous change in single RyR2 $P_O$. *B*, the mean probability of NOX2 being in the activated state ($\pi_X^A$) during a 10 s stretch of varying magnitudes (i.e. 0, 3, 6, 8 and 10%) and frequencies (i.e. 0, 1 and 2 Hz). Note that a 0 Hz stretch indicates a static, 'stretch-and-hold' protocol. *C* and *D*, number of $Ca^{2+}$ sparks ($cell^{-1}$ $s^{-1}$) during a static (*C*) and a cyclical (*D*) stretch protocol.

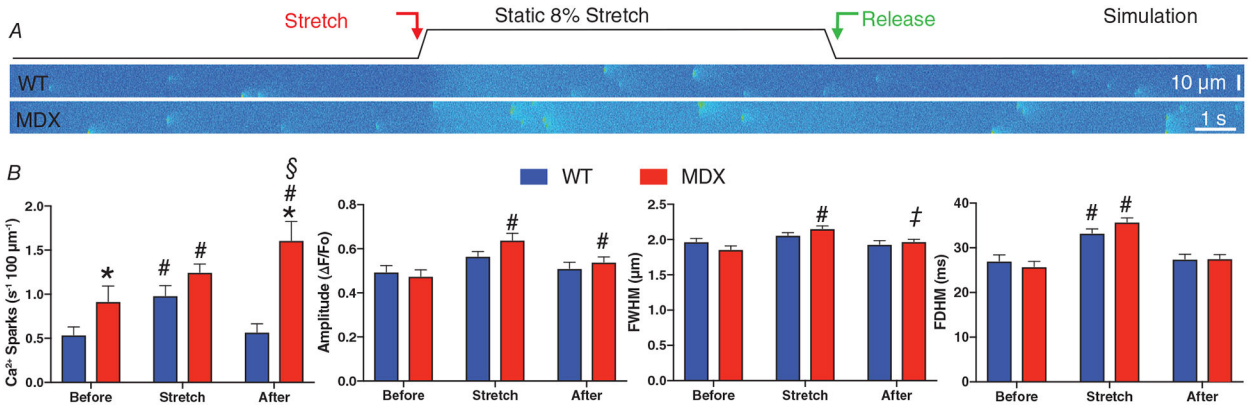


**Figure 6. Modelling captures stretch-dependent $Ca^{2+}$ spark behaviour in healthy and dystrophic heart**

*A*, representative simulations of transverse confocal linescans for WT and MDX VCMs with an 8% stretch imposed at the red arrow. *B*, $Ca^{2+}$ spark frequency, amplitude, FDHM and FWHM before, during and after a static, 8% stretch. Note, simulated transverse linescan frequencies have been adjusted (i.e. divided by 3) to enable direct comparison to experimental longitudinal linescan measures based on an average 600 nm and 1.8 $\mu$m inter-CRU distance, respectively. *C*, simulations of transverse confocal linescans for WT and MDX VCMs exposed to a cyclic, 2 Hz, 10 % stretch. Conditions as follows, WT (WT); MDX (MDX); MDX with 2-fold increase in X-ROS (MDX+); and MDX modified with 'normalized' (i.e, equivalent to WT levels) X-ROS components (MDX−). Statistics: MDX compared to WT ($^{*}P < 0.05$), Stretch compared to Before ($^{\#}P < 0.05$), After compared to Before ($^{\S}P < 0.05$), and After compared to Stretch ($^{\ddagger}P < 0.05$).

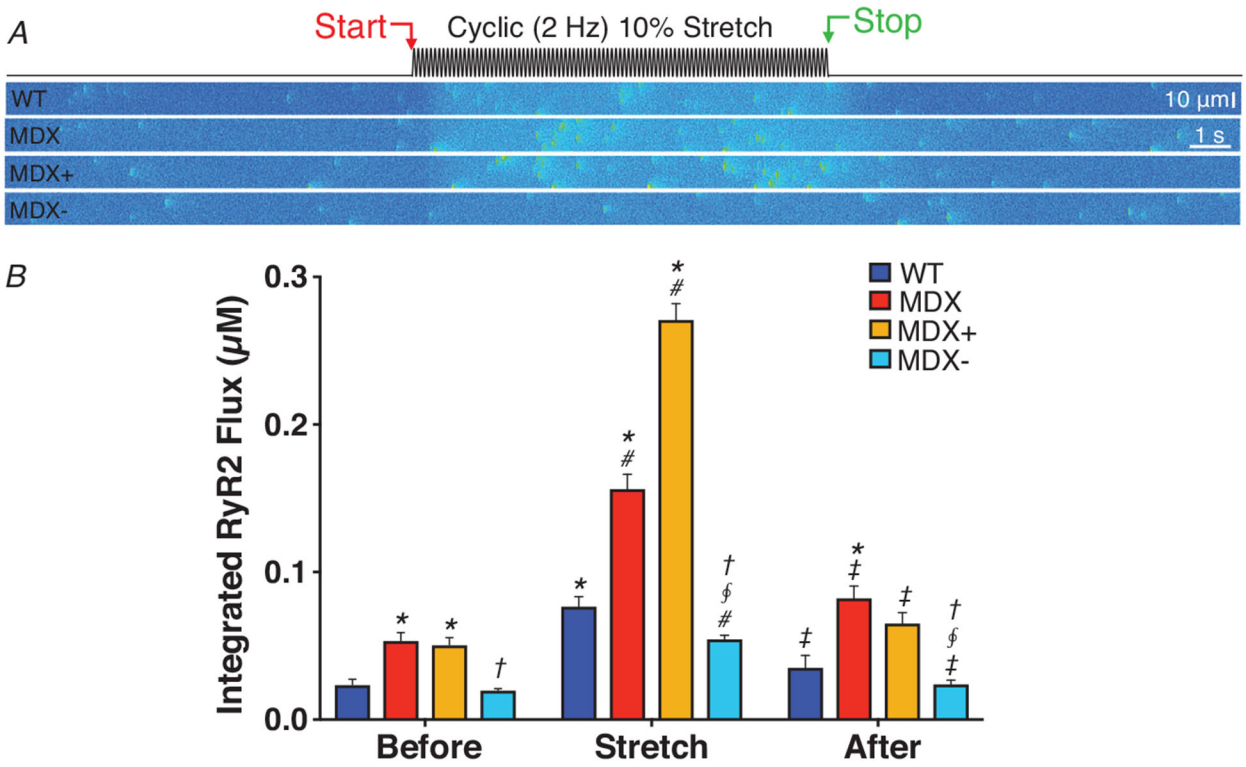


**Figure 7. MT densification drives SR $Ca^{2+}$ leak towards arrhythmogenic levels during cyclic stretch in heart**

*A*, simulations of transverse confocal linescans for WT and MDX VCMs exposed to a cyclic, 2 Hz, 10% stretch. Conditions as follows, WT (WT); MDX (MDX); MDX with 2-fold increase in X-ROS (MDX+); and MDX modified with 'normalized' (i.e, equivalent to WT levels) X-ROS components (MDX−). *B*, quantification of RyR release flux. Statistics: Test group (i.e. MDX, MDX+, MDX−) compared to WT ($^{*}P < 0.05$) within each condition (i.e. Before, Stretch, After), MDX− compared to MDX+ within each condition ($^{\S}P < 0.05$), MDX− compared to MDX within each condition ($^{\dagger}P < 0.05$), Stretch compared to Before ($^{\#}P < 0.05$), and After compared to Stretch ($^{\ddagger}P < 0.05$).

**Table 1.**

Select model parameters

| Parameter | Description | Value (WT) | Reference/constraint |
|---|---|---|---|
| $g_{saca}$ | Whole conductance for stretch-activated $Ca^{2+}$ influx pathway | 1500 pS | Fig. 3 |
| $\beta_m$ | MT strain scalar | 10 | N/A |
| $\beta_0$ | Minimal MT stain factor | 0.01 | N/A |
| $\beta_1$ | MT strain normalizing factor | 0.1 | N/A |
| $\beta_\eta$ | Cooperativity factor for MT strain | 2 | N/A |
| $\rho_{MT}$ | Unitless MT density | 1 | N/A |
| $\rho_{NOX2}$ | Unitless NOX2 density | 1 | N/A |
| $\rho_{WT}^{o}$ | Basal oxidization factor for WT | 0 | Figs 3 and 4 |
| $\rho_{MDX}^{o}$ | Basal oxidization factor for MDX | 0.08 | Figs 3 and 4 |
| $k_{da}$ | NOX2 rate constant | 0.2 $s^{-1}$ | Prosser et al. (2011, 2013b) |
| $k_{ar}$ | NOX2 rate constant | 0.25 $s^{-1}$ | Prosser *et al.* (2011, 2013b) |
| $k_{rd}$ | NOX2 rate constant | 1 $s^{-1}$ | Prosser *et al.* (2011, 2013b) |
| $k_{ad}$ | NOX2 rate constant | 1 $s^{-1}$ | Prosser *et al.* (2011, 2013b) |
| $k_{dr}$ | NOX2 rate constant | 1 $s^{-1}$ | Prosser *et al.* (2011, 2013b) |
| $k_{ra}$ | NOX2 rate constant | 0.05 $s^{-1}$ | Prosser *et al.* (2011, 2013b) |
| $k_{12}$ | RyR2 opening rate | 0.2 $\mu M^{-\eta}$ $s^{-1}$ | Wescott *et al.* (2016) |
| $k_{21}$ | RyR2 closing rate | 425 $s^{-1}$ | Wescott *et al.* (2016) |
| $A_p$ | SERCA density | 50 $\mu M$ | Wescott *et al.* (2016) |
| $I_{ncx}^{1}$ | Maximal NCX current | 500 pA | Wescott *et al.* (2016) |

See Wescott *et al.* (2016) for additional parameters.

**Table 2.**

Model parameters altered in MDX

| Parameter | Fold change in MDX | Reference/constraint |
|---|---|---|
| $\rho_{MT}$ | 1.5 | Fig. 2 |
| $\rho_{NOX2}$ | 2.5 | Fig. 2 |
| $A_p$ | 1.5 | Fauconnier *et al.* (2010), Wang et al. (2015) |
| $v_{ncx}$ | 1.2 | Fauconnier *et al.* (2010), Wang *et al.* (2015) |